Tidal Triggering of Microseismicity at the Equatorial Mid-Atlantic Ridge, Inferred from OBS Network

K. Leptokaropoulos[1], N. Harmon[1], S. P. Hicks[2], C. Rychert[1], D. Schlaphorst[3] and J. M. Kendal[4]

[1] Ocean and Earth Science, University of Southampton, Southampton, UK.

[2] Department of Earth Science and Engineering, Imperial College London, London, UK.

[3] Instituto Dom Luiz (IDL), Faculdade de Ciências, Universidade de Lisboa, Lisbon, Portugal.

[4] School of Earth Sciences,University of Oxford, Oxford, UK.

Corresponding author: Konstantinos Leptokaropoulos (K.Leptokaropoulos@soton.ac.uk)

Key Points:

- Tidal triggering is investigated for a microseismicity dataset from the equatorial Mid-Atlantic ridge
- Seismicity rates are increased and b-values are decreased during and towards low tides
- Results suggest influence of additional triggering factors such as fatigue and/or presence of a shallow magma chamber beneath the ridge

Abstract

The gravitational pulls from the moon and the sun result in tidal forces which influence both Earth's solid and water mass. These stresses are periodically added to the tectonic ones and may become sufficient for initiating rupture in fault systems critically close to failure. Previous research indicates correlations between increased seismicity rates and low tides for mid-ocean, fast-spreading ridges in Pacific ocean. Here, we present a microseismicity dataset (4719 events) from an Ocean Bottom Seismometer (OBS) network at the equatorial Mid-Atlantic Ridge, suggesting a significant correlation between seismic potential and tidal forces. We show that low as well as decreasing ocean water level results in elevated seismicity rates and lower b-values, translated into considerably increased probabilities of stronger event occurrence at or towards low tides. In addition, seismic bursts (enhanced activity rate clusters), occurring at rates fairly above the reference seismicity, are exclusively present during either high extensional stresses or high extensional stress rates. Our results exhibit remarkable statistical significance, supporting the previous findings for tidal triggering at low tides within normal-faulting regimes and extending the range of observations to slow-spreading ridges. Observed triggering of slip on low angle faults at low tides is predicted by Coulomb stress modelling. The triggering of slip on high angle faults observed here, is not easily explained without another factor. It may be related to fatigue and/or the presence of a shallow magma body beneath the ridge, as suggested by previous seismic imaging in the region.

1 Introduction

Oceanic plates constitute the major part of Earth's lithosphere, and mid-ocean ridges (MOR), the active boundaries of two divergent oceanic plates play a major role in global plate tectonics. New lithosphere is created along oceanic spreading centres by a combination of tectonic and magmatic processes, as molten rock emerges from the upper mantle beneath (Hofmann, 1997). Recently, Agius et al. (2021) showed that deep material transfer from lower to upper mantle is also linked to spreading processes along the equatorial Mid-Atlantic Ridge (MAR), thus ridge upwellings may compensate slab downwellings in subduction zones. The MAR is Earth's longest mountain chain extending from the Arctic down to the Bouvet Triple Junction in South Atlantic and is characterized as a slow spreading ridge (<40mm/yr). Volcanic activity is also evident as well as shallow seismicity, often occurring as swarms (e.g. Sykes, 1970). This long belt is not continuous but fragmented by a system of dextral and sinistral transform faults (TF), perpendicular to the ridge (MacDonald, 2001). Seismicity along the MAR provides evidence for the nature of the processes that govern the composition and dynamics of the oceanic lithosphere. Normal faulting is observed predominantly along the ridge, with earthquake magnitudes rarely exceeding M_W=6.0. Strike-slip faulting with one nodal plane parallel to the TF strike is the dominant mechanism along the TFs.

Our study area is a segment of the equatorial MAR located at approximately 1^{o}S and 16^o W (Figure 1), between the Chain and Romanche TFs. Both TFs and the ridge segment they offset were previously mapped, although more for physical oceanographic purposes (e.g. Mercier and Morin, 1997; Mercier and Speer, 1998). In March 2016, 39 ocean bottom seismometers (OBS) were deployed at both sides of the MAR, centred on the Chain Transform Zone (CTZ), under the framework of the PI-LAB (Passive Imaging of the Lithosphere-Asthenosphere Boundary) and the EURO-LAB experiments (Experiment to Unearth the Rheological Lithosphere-

Asthenospehre Boundary). The network operated for 1 year and the data acquired were used, in combination with other geophysical measurements, in a variety of studies focused on sediment structure (Agius et al., 2018; Saikia et al., 2020), infragravity wave sources (Bogiatzis et al., 2020), a multidisciplinary marine geophysical investigation of the active transform valley, the adjacent spreading segments and oceanic lithosphere (e.g. Harmon et al., 2018, 2020; Wang et al., 2020; Rychert et al., 2020), and a high-resolution study of a M_W=7.1 earthquake on the nearby Romanche TF (Hicks et al., 2020). Here, we use the data gathered within the duration of the PILAB experiment, in order to study the properties and triggering mechanisms of microseismicity that occurred in the equatorial segment of the MAR.

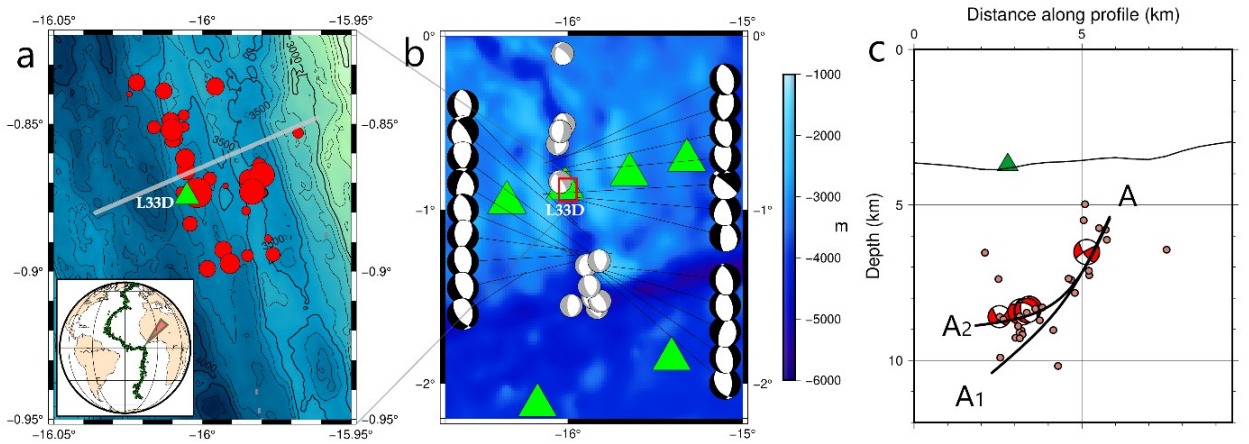

Figure 1. (a). Bathymetric map of the study area. The red circles indicate the seismicity templates used to compile the catalogue used in the study. The inset map indicates the location of the study area in Atlantic ocean (red arrow) and show MAR global seismicity since 1964 (green circles) (data from isc.ac.uk/). The grey line indicates the cross-section shown in (c). (b). Broader area showing the ridge segment (deep blue line with approximately north-south orientation). The red rectangle shows the study area, magnified in (a). The focal mechanisms from GCMT (black) and this study (grey) are shown as lower hemisphere projections. Green triangles denote the location of OBS stations in both (a) and (b) and the closest station, L33D is also noted. (c). Double difference locations of selected events, plotted along a ridge-perpendicular cross-section, suggesting possible reactivations of a west-dipping normal fault. Plausible high angle (Line A-A1) or listric (Line A-A2) fault geometries are shown in (c). The available focal mechanisms projected onto the cross-section, and L33D station (green triangle) are also depicted.

Several of the proposed mechanisms of seismic activity across MORs are related to the thermal profile and regard frictional weakening occurring in high-temperature (e.g. geothermal) extensional regimes (e.g. Hough and Kanamori, 2002), hydrothermal circulation (e.g. Behn et al., 2007), and hydrothermal alteration (serpentinization) which considerably lowers rock strength (e.g. Escartin et al., 2001). In addition, oceanic faults are subjected to a permanent seawater overburden, which produces considerable tidal effects. The solar and lunar gravitational interaction with the Earth induces oscillatory stresses at semi-diurnal (~12h), diurnal (~24h) and even longer periods (e.g. fortnightly, ~14.7 days). Although, the tidal stresses (kPa) are lower by ~3 orders of magnitude compared to the tectonic stresses (MPa), rate of tidal stressing may be comparable to or exceed that of tectonic stressing by up to two orders of magnitude (Heaton,

1975; Wilcock et al., 2016). In addition, since tides are periodic and their effect can be stacked in time, they provide a useful tool for investigating potential earthquake triggering, if present.

There are several studies suggesting tidal triggering at MORs (e.g. Wilcock, 2001; Tolstoy et al., 2002; Stroup et al., 2007; Bhatnagar et al., 2015; Wilcock et al., 2016; Tan et al., 2019). These studies have only focussed on intermediate (Juan de Fuca) and fast (East Pacific Rise) spreading MORs and less attention has been paid to slow spreading ridges such as MAR. Although there are some microseismicity studies for various MAR segments (e.g. Gravemeyer et al., 2013; Horning et al., 2017; Parnell-Turner et al., 2017; 2020), temporal variations in seismicity, such as tidal effects and triggering mechanisms across MAR have not been fully investigated. Tidal pressure was shown to modulate high temperature hydrothermal discharge at the Lucky Strike deep sea vent field, although seismicity was only briefly discussed (Barreyre et al., 2014).

Summarising the findings of the previous research, there are four major characteristics of tidal triggering in oceanic environments:

1) *Tectonic setting*. Tidal triggering has been identified in normal (e.g. Tanaka et al., 2002; Tsuruoka et al., 1995; Scholz et al., 2019) and reverse (e.g. Cochran et al., 2004; Ide et al., 2016; Tanaka et al., 2002;) faulting regimes, whereas it is essentially absent in any strike-slip fault systems (e.g. Tanaka et al., 2002; Tsuruoka et al., 1995; Vidale et al., 1998).

2) *Tidal characteristics*. Ocean tides dominate, inducing stresses an order of magnitude larger than the solid earth tides (Wilcock, 2009; Cochran et al., 2004; Tsuruoka et al., 1995). An exception is the 9o50'N on the East pacific rise, which is located within an ocean tidal node, resulting in the dominance of solid earth over ocean tides (Bhatnagar et al., 2015; Stroup et al., 2007).

3) *Timing*. Vertical tidal stress also dominates and is in phase with the ocean tides (e.g. Wilcock, 2001; Scholz et al., 2019), such that the vertical component (directly connected to ocean height) can be mainly considered.

4) *Optimum receiver fault geometry*. Particularly at MORs, triggering in normal faults is associated with low tides, which correspond to the maximum extensional stress (e.g. Tolstoy et al., 2002; Tsuruoka et al., 1995; Wilcock et al., 2016). This is genereally inconsistent with the predicted Coloumb stress at low tides for high angle normal faults. However, it could be consistent with Colomb stresses that would unclamp (Wilcock et al., 2016) low angle normal faults, i.e., that could exist if the MOR faults are listric in shape. Alternatively, additional influences such as magmatic expansion from below have been suggested (Sholtz et al., 2019).

In this study we use the seismicity data acquired by the PI-LAB and EURO-LAB projects to investigate the role of tides as a triggering mechanism of microseismicity along a segment of the equatorial MAR. We investigate the correlation between ocean tide phase and amplitude with the occurrence of seismicity. Then, we identify seismic sequences characterised by enhanced activity rates (i.e. temporal clusters) separated by time periods in which seismic activity falls well below the reference seismicity level. We also demonstrate how the magnitude distribution of seismicity is influenced by tidal fluctuations. Finally, we interpret the results in terms of Coulomb stress changes and extract information on frictional and hydraulic properties of the lithosphere in the close vicinity of ridge.

2 Materials and Methods

2.1 Seismicity Data

We use continuous waveform data from the PI-LAB OBS stations and apply 'lassie' (Heimann, 2017), a stack-and-delay based waveform coherence detector, to find and locate seismic events. In this method, coherency is mapped using a smooth characteristic function calculated from normalised envelopes. We specifically target events within a radius of ~25 km from station L33D, which is located in the axial valley (Figure 1). Such a limited radius was used to ensure that the events were located in the vicinity of L33D with robust depth resolution, and also to minimise the likelihood of detecting seismicity along the adjacent TFs.

Following manual picking of P- and S-wave arrival times in detected events, we then relocate these events with a probabilistic non-linear approach using the NonLinLoc software (Lomax et al., 2000). We use a 1-D V_p model based on CRUST1.0 (Laske et al., 2013). We select a fixed V_p/V_s ratio of 1.74 based on a linear fit to a modified Wadati plot (e.g. Chatelain et al., 1980). This yielded a total of 48 well-located events (azimuthal gap <220°; >4 P-wave picks; >3 S-wave picks; maximum depth error, within 68% confidence interval, <5 km). The average RMS residual of these events is ~0.08 s, suggesting well-constrained locations and minimal unmodelled velocity deviations from the 1-D approximation. We compute event magnitudes by taking the three-component maximum amplitude and computing single-station local magnitudes (M_L) at station L33D using the relationship derived by Crawford et al. (2013) for the Lucky Strike volcano area on the MAR.

For higher-precision earthquake locations, we use the double-difference method (Waldhauser & Ellsworth, 2000) that uses our phase arrival times and higher-precision cross-correlation measurements for P- and S- waves on a window of 2.5-18 Hz bandpass-filtered data starting 0.1 s before and ending 0.2 s after our picked arrival time. We allow a maximum cross-correlation lag of 0.1 s and a minimum allowed cross-correlation coefficient of 0.4. This double-difference relocation resulted in a single cluster of 34 events with a mean depth error of ~200 m indicating a distinct group of events lying at 5-10 km depth beneath sea level (Figure 1c). The shallower events, to the side of the axial valley, appear to form a lineation in seismicity, which dips at a moderate angle to the west. A tight cluster of events lies directly beneath the axial valley at 8-10 km depth below sea level. Visual analysis of waveforms at ridge station L33D showes that recordings of small, local seismic events (S-P differential time of <2 s) are very common, with tens of these signals showing up in a typical day. However, many of these events cannot be identified on other stations, as would be needed for network-based detection and relocation.

To further investigate microseismicity along the ridge segment, we mostly rely on single-station detection at L33D. We use waveform template matching to study the ridge microseismicity, which allows detection of events within noise (e.g. Gibbons & Ringdal, 2006). From three-component waveforms of the double-difference relocated events, we form event templates. We used our catalogue of 48 events as templates used for the matched filter-detection using the EQcorrscan software package (Chamberlain et al., 2018). Templates are bandpass-filtered between 2 and 20 Hz, which includes much of the energy of these local seismic events, and minimises the effect of ocean noise. Templates are 1.4 s

long, beginning 0.1 seconds before the picked arrival time. P-wave templates are constructed on the vertical component, whereas S-waves come from the horizontal components. Thresholding is based on the mean-values of cross-correlations from each of L33D's components. Visual analysis of waveforms from a subset of detected events shows that an average channel correlation detection threshold of 0.65 is suitable. This value is similar to other studies using single-station template matching (e.g. Vuan et al., 2018). We then check for, and remove, duplicate detections (within 20 s) and select the template detection with the greatest mean cross-correlation value. This workflow led us to the identification of 4,719 events with magnitudes range from M_L -1.4 to M_L 4.0.

The moment tensor solutions are calculated using the local seismicity catalogue. The hypocentre depths and focal mechanisms are computed using Bayesian-bootstrap time-domain deviatoric moment tensor inversion in Grond (see Heimann et al., 2018 for further details). The data is inverted in the frequency range of 12-25 s. The previously derived lateral location is kept fixed and for the inversion only the vertical traces are used. The solutions presented in this work represent the double-couple component of the focal mechanism, since the station coverage is not able to resolve potential non-double couple faulting components. The uncertainties in centroid depth and focal mechanism parameters are representations of the probability density functions derived from bootstrapping chains. Due to noise and event magnitude constraints, focal mechanisms could only be obtained for five of the events in the study area (Figure 1c) and twelve events along the entire ridge segment (Figure 1b).

2.2 Tidal Stresses

The SPOTL software (Agnew, 1997) is used to calculate solid earth tides as well as ocean loading with the global ocean tide model TPXO72.2010, produced by Oregon State University (see Egbert and Erofeeva, 2002). The predicted tidal heights are estimated by incorporating the tidal constituents M2, N2, S2, K2, K1, P1, O1 Q1 and M4 (Agnew, 1997 and references therein). The vertical stress can be then derived directly from the ocean tide height, given the water density, ρ, and the gravity acceleration, g, as:

$$\Delta\sigma_Z = g\rho h \qquad (1)$$

Whereas the horizontal stresses induced by ocean tides ($\Delta\sigma_{Xo}$ and $\Delta\sigma_{Yo}$), assuming uniaxial strain, can be expressed as:

$$\Delta\sigma_{Xo} = \Delta\sigma_{Yo} = \frac{\nu}{1-\nu}\,\Delta\sigma_Z \qquad (2)$$

Where, ν is the Poisson ratio. The corresponding horizontal stresses due to the solid earth tides ($\Delta\sigma_{Xe}$ and $\Delta\sigma_{Ye}$) are:

$$\Delta\sigma_{Xe} = \frac{E}{1-\nu^2}(\Delta\varepsilon_X + \nu\Delta\varepsilon_Y),\ \Delta\sigma_{Ye} = \frac{E}{1-\nu^2}(\Delta\varepsilon_Y + \nu\Delta\varepsilon_X) \qquad (3)$$

where $\Delta\varepsilon_X$ and $\Delta\varepsilon_Y$, are the horizontal tidal normal strains, calculated by SPOTL and E, is Young's modulus. Solid earth tides do not alter the vertical stress right below the ocean floor and thus, we assume that equation (1) is a sufficient approximation of vertical stress change at shallow depths (e.g. Wilcock, 2009). The horizontal stresses induced by ocean tides have

amplitudes comparable to the corresponding ones produced by solid earth tides and they usually lag almost half a cycle. As a result, they compensate each other and thus, total horizontal stresses are at most of the time roughly an order of magnitude smaller than the vertical stress induced by the water column fluctuations (Figure S1; Figure S2). Given a fault with dip, δ and rake, λ, the contribution of tidal loading changes in the Coulomb failure stress, ΔCFS, (e.g. Harris, 1998) is given as:

$$\Delta CFS=\Delta\tau+\mu(\Delta\sigma_n+\Delta P) \quad (4),$$

whereas the shear stress acting on the fault plane, Δτ, can be expressed as:

$$\Delta\tau=\Delta\sigma_Z\left(\frac{2\nu-1}{1-\nu}\right)sin\lambda\cdot sin\delta\cdot cos\delta \quad (5),$$

the normal stress can be written as:

$$\Delta\sigma_n=\Delta\sigma_Z\left(\cos^2\delta+\frac{\nu}{1-\nu}\sin^2\delta\right) \quad (6),$$

and the difference in pore pressure, ΔP, under undrained conditions is:

$$\Delta P=-B\frac{\Delta\sigma_{jj}}{3} \quad (7),$$

where, σ_{jj}, is the stress tensor trace, μ is the friction coefficient and B is the equivalent for rocks of the Skempton (1954) coefficient, β, that was originally determined for soils (Rice and Cleary, 1976). We use the typical sign convention, with δ being positive downwards and λ being positive for uplift of the hanging wall (i.e. for thrust faulting). For ΔCFS, positive values indicate that slip is promoted at low tides and vice versa.

Although it is expected that normal faulting prevails within the extensional regime across the ridge, it has been shown that focal mechanisms can be far more variable and complex (e.g. Parnell-Turner et al., 2017). A limited number of focal mechanism solutions for the equatorial MAR segment are available (Figure 1b), and even less for our study area (Figure 1c). In addition to computational uncertainties resulting from the network coverage, there is also uncertainty in terms of which of the two nodal planes is the fault plane. For these reasons we proceed to our analysis by taking into account tidal height and tidal phase, initially disregarding the stress calculations (e.g. Wilcock, 2016; Scholz et al., 2019). In later sections we demonstrate ΔCFS calculations for various δ, λ, μ and B combinations, effectively allowing us to determine plausible planes optimally oriented for failure at high and low tides.

For the calculations we assume $V_P/V_S=1.74$, leading to a Poisson ratio $\nu\sim0.25$. The ocean water density is set to 1030kg/m^3 and the gravitational acceleration at the equatorial latitude is 9.781m/s^2. A Young modulus of $E=1.1\cdot10^{11}$Pa is selected. These parameter values result in root mean square values of $\Delta\sigma_Z$=3.41kPa, $\Delta\sigma_Y$=0.75kPa and $\Delta\sigma_Y$=0.47kPa, showing that vertical stresses clearly prevail over the horizontal ones (Figure S1). In addition, the maximum stress rates (from high to low tide or vice versa) ranges between ~0.007 to 0.015 MPa/6h, corresponding to 70cm and 150cm difference in the water level, respectively, occurring during each semidiurnal tidal half-cycle. For the ΔCFS calculations, we considered $0^o\leq\delta\leq90^o$, $0^o\leq\lambda\leq-180^o$, $0.6\leq\mu\leq0.7$ and $0.25\leq B\leq1.0$.

2.3 Tidal Phase

Given that the semidiurnal tidal period is ~12h 25', the ocean height is calculated separately, at the epicentral coordinates of each event for a time span ranging from 7h before to 7h after the event occurrence time. By doing this we ensure that a complete tidal cycle is considered and a phase within the cycle can be assigned to each event. The time step for subsequent calculations is 72 seconds. Since the magnitudes of solid Earth tides are secondary and they do not change abruptly in space, average values at the centre of the study area are calculated for the entire study period with the same time step of 72 seconds.

We define the phase, ϕ, relative to the low tide, which is found to promote failure in extensional regimes (Scholz et al., 2019 and references therein). In other words, 0° corresponds to the low tide (minimum water height), ±90° correspond to zero tidal height (average water level) whereas +180° and -180° correspond to the subsequent and preceding high tides, respectively (Figure 2). Note that extensional stress (tidal height below zero) occurs at -90°<ϕ<90° maximized at 0°, whereas extensional stress rate occurs at -180°<ϕ<0° maximized at -90°. After defining the phase of each event, we count the number of events that occurred at specified phase bins to identify whether there is a preference for particular phase ranges.

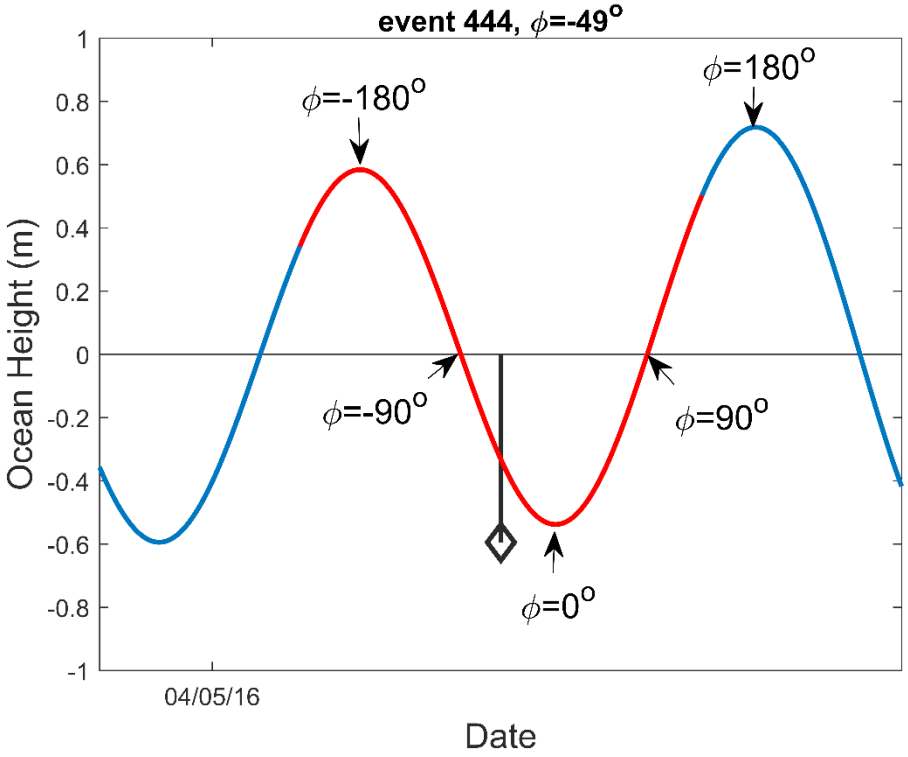

Figure 2. Example of phase, ϕ, determination. The continuous curve shows the tidal amplitude (ocean height) as a function of time, at the epicentral coordinates of the selected event, the occurrence time of which is indicated by the stem. The zero-amplitude baseline is depicted by the horizontal line. The phase count starts at minimum height, indicated as 0°. The positive phases go rightwards, corresponding to increasing ocean height (compressional stress rate), whereas negative phases go leftwards corresponding to decreasing ocean height (extensional stress rate). In the area below the baseline, where |ϕ|<90° negative ocean height occurs (extensional stresses) while in the area above the baseline, with |ϕ|>90° positive ocean height occurs (compressional stresses). The red curve highlights one tidal cycle centred at the event

occurrence time, at -49° phase. The zero ocean height (~ϕ=±90°) and maximum ocean height (~ϕ=±180°) points are also arrow-indicated in the figure. The horizontal span is roughly 1 day.

In order to quantify the significance of the results, we perform the commonly applied Schuster (1897) test, which calculates the probability, p_s, that the occurrence times of the events, introduced as phase angles of a specified period, are randomly distributed around the unit circle. In doing so, parameter R, is defined as:

$$R^2=\left(\sum_{i=1}^{N}\cos\phi_i\right)^2+\left(\sum_{i=1}^{N}\sin\phi_i\right)^2 \quad (8)$$

With ϕ, being the phase angle of the i^{th} earthquake in a population of N earthquakes. Then, the probability that a given phase distribution is random reads:

$$p_S=e^{\frac{-R^2}{N}} \quad (9)$$

The lower the p_S, the higher the significance to reject the null hypothesis of random phase distribution. In other words, small p_S, indicates that there is a preference of events to concentrate near particular phase angles, implying a possible causative relationship between tides and earthquake occurrence.

2.4 Magnitude Distribution

We investigate the tidal effect on seismic sequences (i.e. temporal clusters) characterized by enhanced seismic activity, which occur at considerably higher rates than the reference seismicity. This part of analysis requires a complete catalogue, since it involves seismicity rates. The Anderson-Darling (Marsaglia and Marsaglia, 2004; Leptokaropoulos, 2020) test (AD-test) is applied for different magnitude cut-off (M_{cut}) values, for verifying whether the magnitudes are drawn from an exponential distribution. The completeness magnitude is selected equal to the magnitude above which the exponentiality hypothesis is not rejected by the AD-test at 0.05 significance. Once exponentiality is verified, the b-value of the Gutenberg-Richter (GR) law is derived by the maximum likelihood estimator (MLE) of Aki (1965), together with its standard error. To quantify the significance of the b-value difference between 2 datasets, we apply the Utsu (1999) test, based on the Akaike Information Criterion (AIC):

$$\Delta AIC=-2\left(N_1+N_2\right)\cdot\ln\left(N_1+N_2\right)+2N_1\cdot\ln\left(N_1+\frac{N_2 b_1}{b_2}\right)+2N_2\cdot\ln\left(N_2+\frac{N_1 b_2}{b_1}\right)-2 \quad (10)$$

Where N_1, N_2 are the number of events and b_1, b_2 the corresponding b-values of the two datasets, respectively. The Utsu test gives the probability, p_u, that two given datasets are drawn from the same population (same b-values), defined as:

$$p_u=e^{-\left(\frac{\Delta AIC}{2}-2\right)} \quad (11)$$

The lower the p_u, the stronger the indication that the b-values of the two datasets differ. Finally, to evaluate seismic potential as the combined effect of seismicity rates and magnitude distribution, we characterize the difference in seismicity between high and low tides in terms of hazard parameters. In particular, the exceedance probability (EP) of a predefined magnitude (M_t) within a fixed time period (T_t) is calculated as:

$$EP=1-e^{-rT_t\left(1-F_m(M_t)\right)} \quad (12)$$

Where, r, is the seismic activity rate above M_C and F_m, is the magnitude Cumulative Distribution Function (CDF). Since the AD-test verifies the exponentiality of magnitude distribution in all cases with $M_{cut} \geq M_C$, we calculate F_m considering the unbounded GR law as:

$$F_m = 1 - e^{-b\left(M - M_C + \frac{\Delta M}{2}\right)}, \text{ for } M \geq M_C, \quad 0, \text{ otherwise} \qquad (13),$$

with ΔM, being the magnitude round-off interval of the catalogue. The EP calculations and their bootstrap confidence intervals (CI) are performed using the SHAPE toolbox (Leptokaropoulos and Lasocki, 2020).

3 Results

3.1 Statistical analysis of seismicity rates and magnitudes within the tidal cycle

We first search for potential correlation between event occurrence times and ocean tide phases, ϕ. Figure 3a shows the distribution of phases for the entire dataset of 4719 events. There is a visible preference of event occurrence at low tides ($-90^o<\phi<90^o$) with the most populated bins corresponding to $-30^o<\phi<30^o$. The binomial test suggests that the difference between the number of events that occurred at low tides (~57%) and those that occurred at high tides (~43%) is significant with $p \sim 10^{-21}$. Moreover, the Schuster test verifies this observation at a very high significance ($p_S \sim 10^{-25}$). We further investigate the magnitude dependence of the tidal triggering, considering diverse magnitude classes shown in Table 1. As the magnitude threshold increases, higher fractions of seismicity tend to occur at low tides (57%-69%), suggesting that stronger events are more prone to tidal triggering. Although the p-value derived from the binomial test declines in each case due to the decreasing sample size, it remains below 0.05 for all cases tested. Following Cochran et al. (2004), the percentage of the excess events, N_{ex}, is defined as $N_{ex} = 100\frac{N_{enc} - \frac{N_{tot}}{2}}{N_{tot}}$, where N_{enc} is the number of events occurring at encouraging ocean tidal height (stress) and N_{tot} the number of total events. In our dataset N_{ex}=7% (2687 out of 4719 events) and gradually increases for higher magnitude thresholds (Table 1). These values for our study area are considerably higher than the ones obtained in other studies (e.g. Cochran et al., 2004; Wilcock 2009) for datasets of comparable sizes.

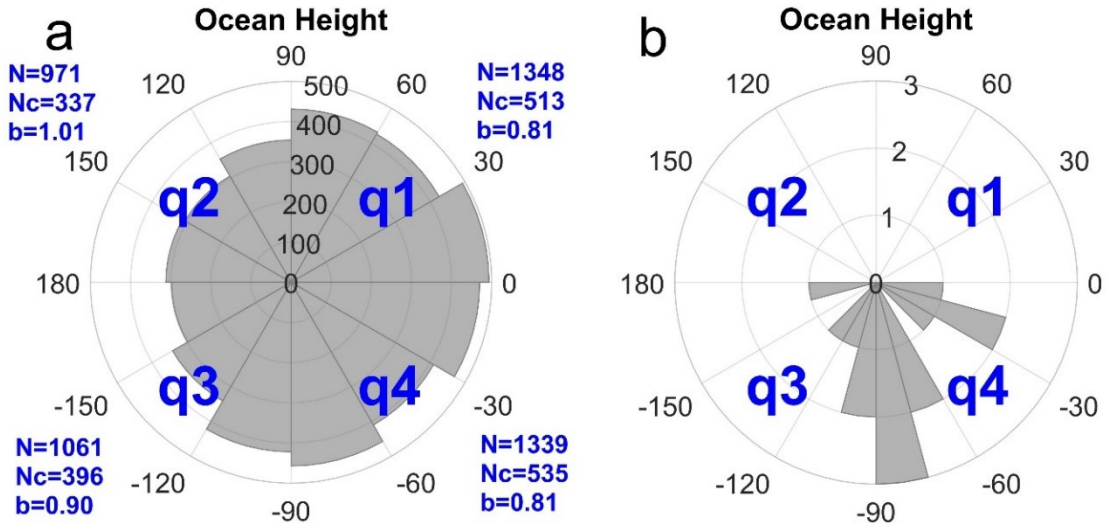

Figure 3. Polar histograms of tidal phases for (a) the entire data of 4719 events and (b) the initiation of the 14 enhanced activity rate clusters (see main text for description). The numbers at the outer circles indicate the phase in degrees, while the concentric circles show the number of events. The blue fonts in (a) represent the number of events (N), the number of events above completeness magnitude, M_C=0.01 (Nc) and the corresponding b-value in each quadrant (q_1-q_4), starting from upper right corner, counter-clockwise.

The lowest number of events as well as the highest b-value are found at the quadrant q_2 ($90^o<\phi<180^o$ see Figure 3a) which corresponds to high compressional stress and compressive stress rate. Quadrant q_3, corresponding to compressional stress but extensional stress rate, demonstrates slightly lower b-value and higher event numbers. Finally, quadrants q_1 and q_4, which correspond to extensional stresses, exhibit almost identical number of events and b-values with each other. The event number in q_1 and q_4 is higher than in the other two quadrants, whereas the b-values are 0.1 and 0.2 units lower that the corresponding values observed in q_3 and q_2, respectively.

Table 1. Statistical properties of the earthquakes distribution that occurred at low tides ($|\phi|<90^o$). The 1st column shows the magnitude cut-off value. The second and third columns show the number of events that occurred at low tides and their percentage to the total data, respectively. The fourth column presents the p-value of the binomial test and the fifth column shows the excess events, N_{ex}, percentage and the corresponding standard deviation (Cochran et al., 2004).

	N with $\|\phi\|<90^o$	% of total	p-value binomial	N_{ex}
All data	2687	56.9%	10^{-21}	6.94% ± 0.72
M>0.0	1048	58.8%	10^{-13}	8.84% ± 1.17
M>1.0	152	61.8%	0.0001	11.79% ± 3.10
M>1.5	69	70.4%	0.0003	20.41% ± 4.61
M>2.0	25	69.4%	0.0144	19.44% ± 7.68
M>2.5	12	75.0%	0.0384	25.0% ± 10.83

Similar results are derived when considering event occurrences versus tidal height. When the total tidal cycles are considered the distribution of normalised frequency is relatively symmetric with respect to the tidal height, and roughly the same number of events occurr at both

low and high tides (Figure S3). However, this symmetry breaks when the occurrence times of the ridge events are considered. There is an excess of events that occur during negative heights (low tide) and an event deficit at high tides, in comparison with the background population of tidal height fluctuation, indicating a clear preference of earthquake occurrence on the ridge at low tides.

The next step is to determine whether tides trigger seismicity with enhanced activity rates (EAR), in the sense of temporal clusters, i.e. sequences occurring at much higher rate than the overall seismic activity (Figure 3b). For that purpose, we first filter the catalogue to include only data above completeness magnitude, M_C, which is found equal to 0.01 (Figure S4). Then, we define such EAR clusters as sequences containing at least 10 events with time difference between subsequent events less than 30 minutes. This way EAR clusters contain a sufficient number of events in order to discriminate from occasionally random, clustered occurrences and on the other hand the duration of the identified clusters remains well below the semi-diurnal tidal half-period of ~6h, in order to unequivocally locate each EAR cluster at a particular phase. 14 such clusters are identified. Note that the mean rate for the events above M_C=0.01 is ~0.22 events/h, whereas the EAR clusters exhibit seismicity rates from 6 to over 40 events/h (i.e. from ~25 to ~200 times higher rates).

Both Table 2 and Figure 4, show that all the 14 EAR clusters identified, exclusively initiated (1st event occurrence time) at negative tidal phase, with a particular preference close to high extensional stress rates (ϕ close to -90^o). 12 out of 14 cluster initiation times (Figure 3b) are located within an ~90^o range (from -106^o to -14^o) in the phase of the tide. The Schuster test p_s=0.0003, verifies that EAR clusters predominantly initiate at a specific phase range. In addition, the phase of all 301 clustered events lies between -165^o and 59^o. This strong preference is verified by a remarkably low p-value from Schuster test equal to $p_s \sim 10^{-62}$. Furthermore, 80% of the clustered events occurred at $-100^o<\phi<15^o$. If we consider the combined influence of the ocean tides and solid earth tides, the phase of the stress is shifted by up to ~40^o counter-clockwise at a few times during the year. However, there is only a slight overall change in the phase of the EAR clusters (Figure S5) and the corresponding p_s values are identical.

Table 2. Properties of the 14 Enhanced Activity Rate (EAR) clusters identified in the study, shown in Figure 4. The first column depicts the cluster ID (in chronological order). 'N', shows the number of events comprizing each cluster. 'T_{cl}', shows the duration of the cluster, whereas 'r', indicates the corresponding activity rate. M_1, shows the magnitude of the first event of each cluster. 'M_{max}' and 'M_{max} rank', depict the magnitude of the strongest event and its rank within each cluster (i.e. the position of the strongest event within the sequence), respectively. 'ΔM', shows the magnitude difference between the two strongest events in each EAR cluster. 'Phase' demonstrates the phase corresponding to the first event of each EAR cluster (beginning of the sequence). The last column shows the MLE of the b-value for each cluster and its standard deviation. The last row indicates the sum for 'N' and 'T_{cl}' and the mean value for 'Phase'.

Cl.	N	T_{cl} *(min)*	r *(events/h)*	M_1	M_{max}	M_{max} rank	ΔM	Phase *(°)*	*b-value*
1	25	52	28.80	2.29	2.97	12/25	0.68	-84.1	0.55±0.11
2	12	120	6.00	0.38	0.73	3/12	0.10	-30.0	1.12±0.32
3	17	24	42.50	0.12	1.93	6/17	0.53	-91.6	0.79±0.19
4	12	51	14.12	2.60	2.60	1/12	1.21	-68.8	0.62±0.18
5	12	70	10.29	3.42	3.42	1/12	2.16	-106.3	0.55±0.16

6	24	104	13.85	1.47	2.41	5/24	0.10	-97.1	0.59±0.12
7	10	71	8.45	0.22	1.20	5/10	0.31	-28.3	1.06±0.33
8	33	144	13.33	1.87	2.76	28/33	0.89	-134.1	0.68±0.12
9	42	203	12.30	0.15	2.13	14/42	0.21	-65.0	0.50±0.08
10	12	92	7.83	1.25	2.23	7/12	0.98	-84.4	0.68±0.20
11	47	169	21.77	1.22	4.00	2/47	2.08	-22.0	0.61±0.09
12	14	71	13.00	2.82	2.82	1/14	0.95	-165.3	0.44±0.12
13	22	98	17.65	0.20	2.27	12/22	0.23	-84.9	0.61±0.13
14	19	130	8.77	0.19	2.84	17/19	1.65	-13.9	0.70±0.16
Sum:	301	23.3 h					***Mean:***	***-82***	

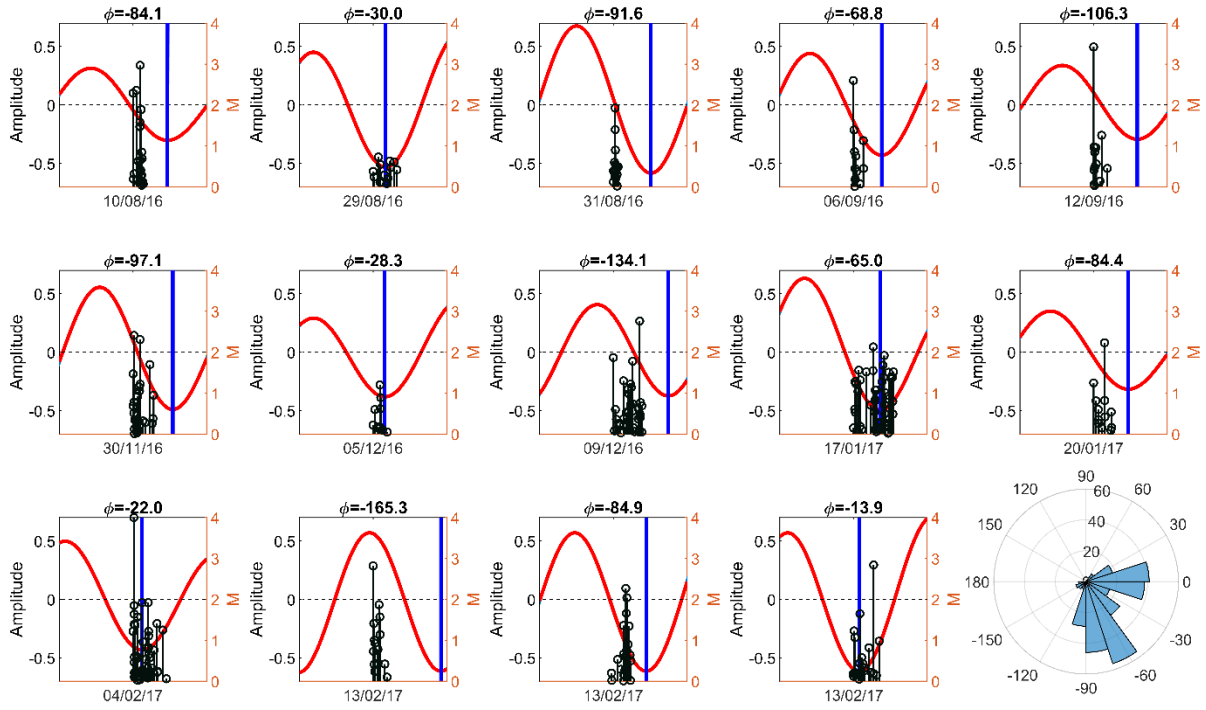

Figure 4. Comparison of the 14 EAR clusters with the tidal cycle. Tidal cycle is indicated by the red curve, centred at the occurrence time of the 1st event of each EAR cluster, the tidal phase of which is written on the top of each panel. Stem plots show occurrence time of the events within each cluster, with the right y-axis indicating their magnitude. The blue vertical line depicts the minimum ocean height, corresponding to $\phi=0^o$. The dashed horizontal line shows the reference ocean level (zero height). The time span on the x-axis is roughly 12h. Note that the last 3 sequences occurred at the same day. The polar histogram at the lower right corner shows the tidal phases of all the 301 events comprising the 14 EAR clusters.

The event magnitude distribution is then investigated. The complete dataset is comprised of 1781 events ($M \geq 0.01$) with a MLE b-value equal to b=0.83±0.02. We search for a difference in magnitude distribution between events that occurred during low tides ($|\phi|<90^o$) and high tides ($|\phi|>90^o$). 1048 events occurred at low tides with a MLE b=0.81±0.03, whereas 733 events occurred during high tides with MLE b=0.85±0.03. Although the two b-values are similar, a closer look at the entire magnitude distribution reveals significant deviations between the two

datasets (Figure S6a). During low tides the b-value is rather stable around 0.80, whilst during high tides the b-value fluctuations are remarkably wider, ranging between 0.85 and 1.00. In addition, for $0.25<M_{cut}<0.45$, the magnitudes at high tides fail to pass the AD test at 0.05 significance, indicating a considerable deviation from GR law. This suggest that either a different physical process leads to such deviation from exponentiality, or that mixed data with diverse properties comprise the high-tide dataset.

Following these results and motivated by a potential influence of stress rate (indicated in Figure 3 and Figure 4), we perform a different division approach, utilizing the combined effect of ocean height and phase. In other words, the magnitude distribution is investigated in terms of stress, but also in terms of stress rate. Such behaviour is shown in Figure 5, where the ocean heights (directly proportional to stress) assigned to each event (with $M \geq 0.01$) are plotted against the corresponding phase. After repeated moving window tests (Figure S7) we are able to identify four characteristic, non-overlapping areas (Figure 5). Area 1 corresponds to high ocean heights (i.e. compression) and it accommodates 504 events with b=0.87. In contrast, Area 3, includes 624 events that occurred at low ocean heights (i.e. extension). This is ~24% more than the events that occurred in Area 1, and in addition, the corresponding b=0.79 is lower than in Area 1. However, during small tidal amplitudes (ocean height from approximately -0.25 to 0.20 m), we can also distinguish 2 domains: Area 2 is characterized by maximum extensional stress rates and accommodates 358 events with b=0.80. Area 4, characterized by maximum compressional stress rates, includes 293 events (Area 2 contains ~22% more events) with b=0.89.

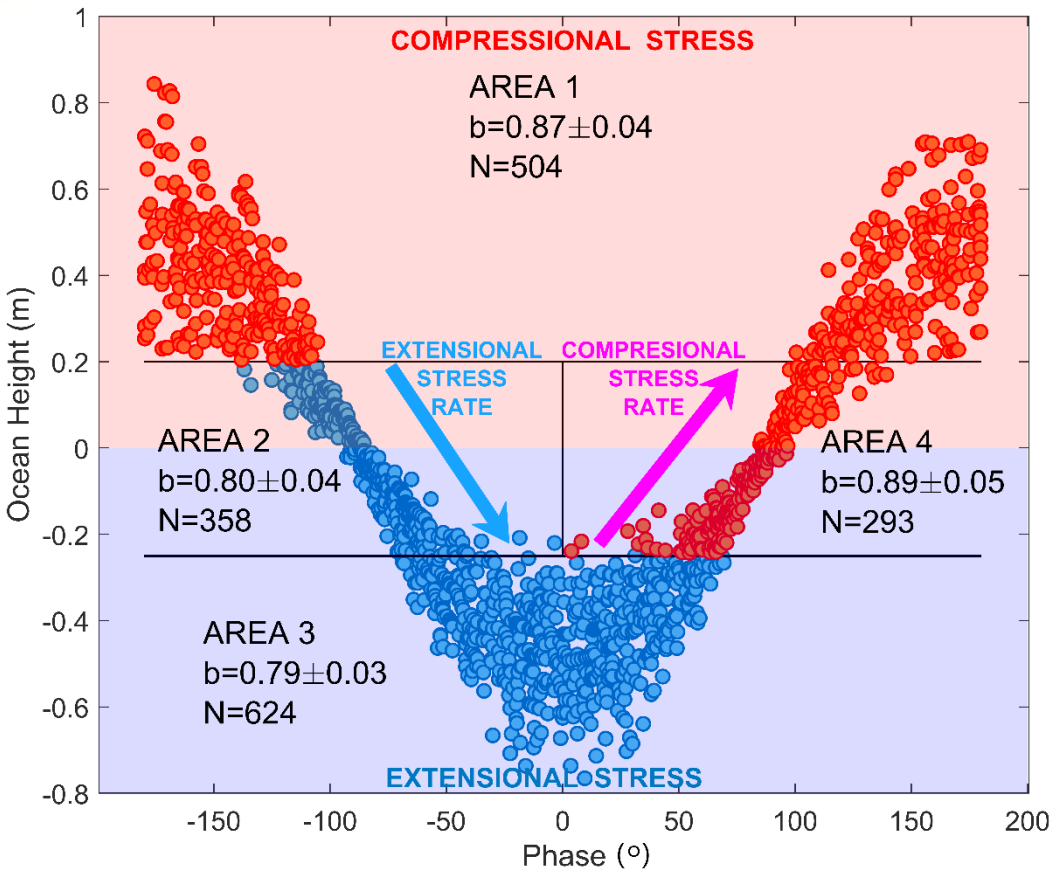

Figure 5. Ocean height plotted against phase for events with M≥0.01 (circles). Red-shaded surface indicates positive ocean height, corresponding to compressional stresses. Blue-shaded surface shows negative ocean height, corresponding to extensional stresses. The blue descending arrow and pink ascending arrow depict the domains of maximum extensional and maximum compressional stress rates, respectively. The black horizontal and vertical lines divide the dataset into the four areas, the event number and b-values of which are noted in the figure. Blue circles represent Group 1, i.e. events occurred during either high extensional stress or high extensional stress rate (Area 3 and Area 2). Red circles represent Group 2, i.e. events occurred during either high compressional stress or high compressional stress rate (Area 1 and Area 4).

Since similar b-values are observed at particular areas of Figure 5, seismicity can be further aggregated in two groups: Group 1 (blue circles in Figure 5) includes Area 2 and Area 3 (high seismicity rates, low b-values), whereas Group 2 (red circles in Figure 5) includes Area 1 and Area 4 (low seismicity rates, high b-values). Group 1 is comprised of 984 events and demonstrates b=0.80±0.025, whereas Group 2 includes 797 events with b=0.88±0.031. The AIC suggests that the difference between these values are statistically significant at 0.05 level. In addition, the plot of b-values as a function of magnitude cut-off (Figure S6b) is far more stable than simply considering events at low/high tides (Figure S6a). This fact is a good indication that the selected datasets in the combined amplitude/phase approach are more homogeneous, comprised of events that follow similar processes. Note that the AD-test for exponentiality is not rejected at any magnitude cut-off for neither Group 1 nor Group 2.

We further assess the tidal effect on seismic potential in terms of combined activity rate and magnitude distribution. In doing so, we calculate exceedance probabilities for specified magnitudes during a predefined time-period. Activity rates are considered to be equal to the corresponding number of events divided by half the duration of the entire dataset, since the whole period of study comprises an almost complete sequence of tidal cycles. In equation (12) we set, T_t=365 days, and we obtain EP_{Group1}=0.275 (95% CI: 0.165-0.433) and EP_{Group2}=0.081 (95% CI: 0.043-0.152) for M≥5.0 and EP_{Group1}=0.050 (95% CI: 0.025-0.097) and EP_{Group2}=0.011 (95% CI: 0.005-0.025) for M≥6.0. The 95% CI do not overlap in both cases suggesting that seismic potential is higher both during low tides and approaching low tides, resulting as a combination of higher activity rates and more frequent large events within the respective magnitude distribution.

Finally, we compare the aggregated magnitude distribution of the EAR clusters, containing 301 events with the remaining, non-clustered seismicity. The result is that EAR clusters demonstrate a MLE b=0.61±0.04 whereas the remaining data above M_C, contain 1480 events with MLE b=0.89±0.02. These b-values statistically differ with each other at very high confidence, according to the AIC, demonstrating $p_u<10^{-7}$. This shows that enhanced seismic activity with considerably higher seismic potential in terms of both activity rates and magnitude distribution is exclusively triggered during either high extensional stress, or high extensional stress rates (i.e. at roughly $-120^o<\phi<30^o$).

3.2 Effect of tidal Coulomb stress on a range of fault planes

Up to this point, we only considered the effect of tidal height and directionality, on seismicity. Here we focus on the tidally induced Coulomb stress changes on various fault plane geometries and parameter values. A commonly applied practice is to use a modified version of equation 4, as

498 $\Delta CFS=\Delta\tau+\mu'(\Delta\sigma_n)$ (14),

499 where μ' is the apparent friction coefficient incorporating pore fluid effects and temporal
500 changes of the effective normal stress (e.g. Linker and Dieterich, 1992). However, this approach
501 is a simplification in an attempt to counterbalance our lack of knowledge regarding the role of
502 pore fluids. The apparent friction coefficient may be written as (Simpson and Reasenberg, 1994):

503 $\mu'=\mu(1-B)$ (15),

504 with B, experimentally determined to take values from 0.47 to 1.0 (Harris, 1998 and
505 references therein), corresponding to a gradual transition from drained to fluid-saturated
506 conditions, respectively. Figure 6 shows the ΔCFS derived by application of equations 4-7 for a
507 variety of fault plane orientations and parameter values. Note that this approach leads to a
508 somewhat different ΔCFS pattern than the one derived by simply setting a μ' value (equation 14,
509 Figure S8).

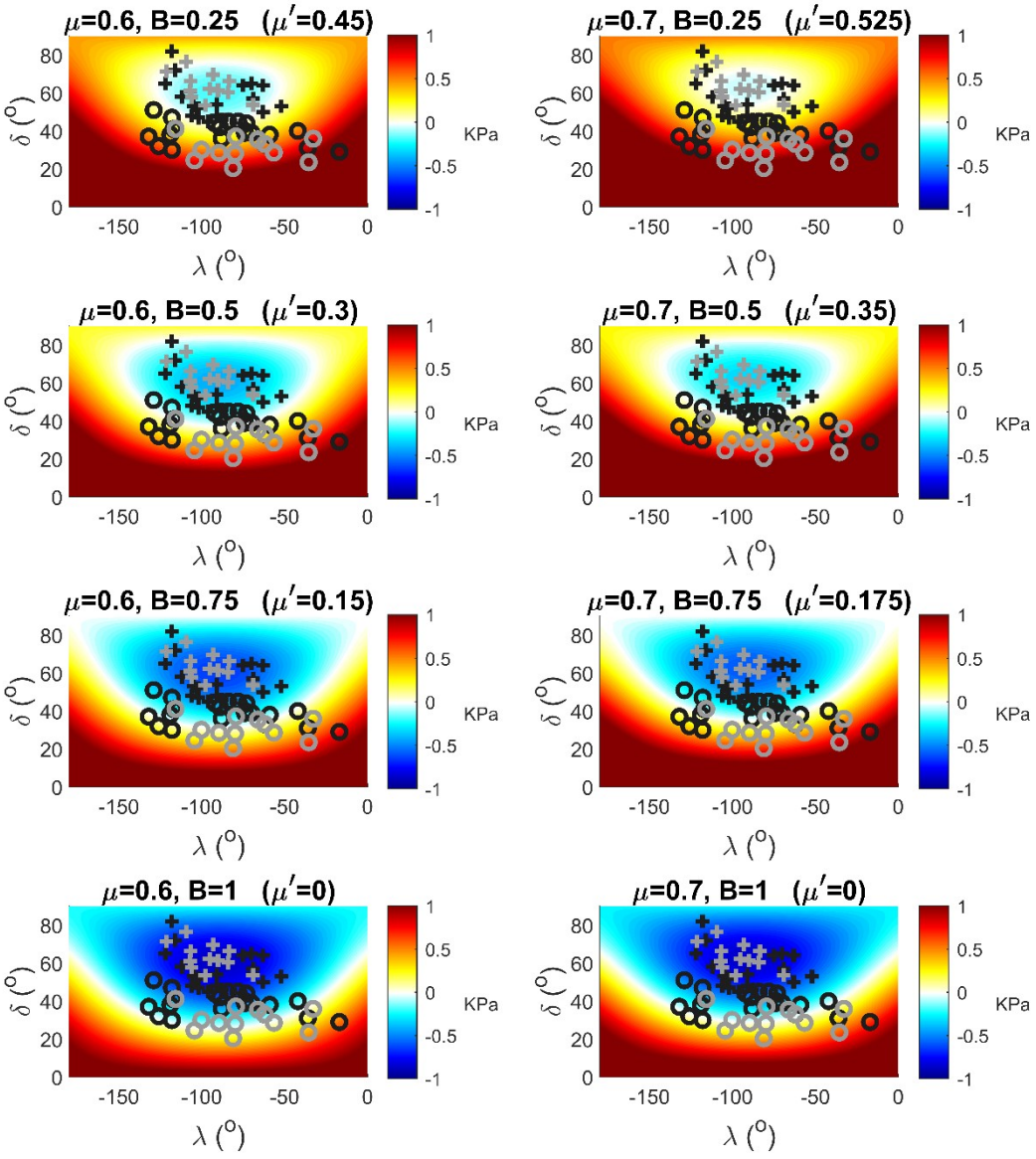

510

511 **Figure 6.** Tidal ΔCFS for dip (y-axis) ranging between 0° and 90° and rake (x-axis) ranging
512 between -180° and 0°. Each frame corresponds to different values of friction coefficient, μ, and

Skempton coefficient, B, (the number in parenthesis denotes the resulting apparent friction coefficient, μ', estimated from equation 15). The warm colours indicate positive ΔCFS (slip is promoted by low tides), while cool colours indicate negative ΔCFS (slip is inhibited by low tides). The available focal mechanisms are also depicted in the plot. Circles correspond to the shallow-dipping planes (<45°) while crosses indicate the steep-dipping planes (>45°). Black and grey marks correspond to the solutions obtained by GCMT and this study, respectively. The colour scale has been saturated at 1kPa for clarity.

Informed choices must be made about the fluid pressure and coefficient of friction for Coloumb stress calculation, which in turn affect the fault dip and rakes that are predicted to promote slip. In terms of fluid pressures, Scholz et al. (2019) state that the lack of a time lag between tidal stress and seismicity occurrence indicates undrained conditions. We also observe this in our study region, indicating undrained conditions. Tesei et al. (2018) compiled a table of friction coefficients, μ for different temperatures and effective normal stresses, showing a wide range for serpentinites between 0.1 and 0.8, with dry samples usually characterised by $0.5<\mu<0.8$ and saturated samples of lizardite and chrysolite being mostly within the range $0.1<\mu<0.4$. For a reasonable choice of Skempton coefficient for unsaturated conditions (0.50 - 0.80, e.g. Harris et al., 1998), the apparent friction coefficient values lies within the range $0.1<\mu'<0.4$. Therefore, although for $\mu'>\sim0.6$ (Figure 6, Figure S8, Wilcock, 2009) failure is promoted at virtually all possible fault planes during low tides, previous research suggests that the apparent friction coefficient values may instead be sufficiently lower.

We test the available focal mechanism solution geometries against various friction values. There are 5 focal mechanisms available for our dataset, two of them indicating normal faulting and the remaining 3 demonstrating a dominant strike-slip component (Figure 1c). These solutions have, however, considerable uncertainties, particularly in the fault dip angle due to the insufficient network coverage. For this reason we further used the available focal mechanisms from the entire ridge segment (Figure 1b). There are 12 focal mechanisms obtained from the OBS recordings, which are fairly similar to each other. On average, they delineate 2 fault planes, one with $\delta=63^o$ and $\lambda=-97^o$, and a second plane with $\delta=30^o$ and $\lambda=-75^o$. The first plane, requires a $\mu'>0.57$ in order to promote failure at low tides, while the second, shallow-dipping plane requires a $\mu'>0.34$ to favour slip during low tides. Results are similar for the 21 focal mechanisms obtained from Harvard Global Centroid Moment Tensor (GCMT), requiring $\mu'>\sim0.57$ and $\mu'>\sim0.43$ for the steep-dipping and the shallow-dipping planes, respectively (Figure 6).

4 Discussion

The Coulomb stress modelling suggests that either slip is triggered on a low angle, low friction fault or that friction is high, in which case slip could be triggered on faults at almost any angle, including high angles. High angle faults require μ' values higher than 0.5 or 0.6, which would suggest drained conditions with B being well below 0.5. This is at the edge of reasonable estimates given our previously discussed observation of a lack of time lag between the tide and seismicity, suggestive relatively undrained conditions (Scholz et al., 2019). In addition, high μ' values are consistent with strong lithosphere. Although the oceanic lithosphere could be variably serpentinised laterally and/or in depth (Davy et al., 2020), oceanic lithosphere is typically assumed to be weak given the abundant presence of lizardite and chrysolite serpentinites (e. g. Escartin et al., 1997; Tesei et al., 2018). So, the high angle triggering is probably less likely.

Alternatively, if the crust is serpentinised along the fault with low friction, slip is promoted at low angles (20^o-40^o). The low angle faults could be associated with detachment faults or the listric base of the high angle faults visible in the nearby seafloor topography (Figure 1c). The detachment faults require a low friction fault rock (Cann et al., 1997). Escartin et al. (2001) showed that even small degree of serpentinization (<15%) can reduce the oceanic strength to that of pure oceanic serpentinite, near the ridge axis. Further weakening may also apply due to increased pore fluid pressures and strain localization caused by the low internal friction of oceanic serpentinites. Therefore, Coulomb stress modelling alone suggests both geometries could be plausible in terms of triggering, although the higher angle case is at the edge of what might be feasible, and probably less likely. In addition, slip at low friction, high angle normal faults should be promoted during high tides, instead.

Additional information can be gathered by the seafloor morphology and vertical distribution of seismic hypocentres. High angle westward dipping fault scarps are visible in the high resolution bathymetry of the region (Fig. 1a) and is consistent with horst and graben type structure that creates abyssal hill fabric. This morphology suggests there has to be high angle faults at shallow depths, in contrast to other locations in the region which show hummocky detachment fault morphology (Harmon et al., 2018). Although the well-constrained relocated data consists of only 34 events, Figure 1c shows that the hypocentres delineate a west-dipping structure, starting with a relatively high angle (>45°) at shallow depths (<8km). The shallowest focal mechanism has a westward dip ~ 57° (Fig. 1c). For the deeper segments, however, the earthquakes distribution does not provide unequivocal conclusions. The fault may either continue to the deeper segments at a relatively high angle (e.g. line A-A1, Figure 1c) or rotate to a lower angle, forming a listric structure (e.g. line A-A2, Figure 1c). Regardless, both options appear relatively listric in structure. Taking this change in angle into account, would suggest high angle slip at shallow depths and lower angle slip at depth. In light of the Coulomb stress modelling, it would mean that the shallow lithosphere is associated with high friction. Although again the degree of serpentinization is not known, it would seem strange given that the entrance way of the water to the lithosphere is presumably via the high angle faults at shallow depth. It suggests another mechanism may be required to explain the triggered slip on the high angle faults. In addition, three out of the five focal mechanisms demonstrate a dominant strike-slip component for the deepest earthquakes, although these solutions are characterized by relatively large uncertainties. Previous studies have shown no evidence of tidal triggering in strike-slip events (e.g. Tanaka et al., 2002). These events may have a significant non-double couple component as often evident in geothermal and volcanic areas (e.g. Miller et al., 1998; Martínez-Garzón et al., 2016; Hrubcová et al., 2021). Our station coverage is not able to resolve potential non-double couple faulting components. This again suggests that another mechanism is required to explain the observed triggered slip.

Another possibility is that triggered slip may be promoted at low tides after incorporating the influence of a magma chamber. In other words, the chamber could inflate owing to its higher compressibility, potentially resulting in a favourable stress field, as has previously been proposed for a fast spreading ridge (Scholz et al., 2019). Deeper strike-slip events, with non-double couple components could be consistent with related dyking events (e.g. Minson et al., 2007). Magma chambers have been rarely imaged at slow spreading ridges like MAR, and it is often assumed that there is insufficient melt production to create an axial magma chamber. However, this could be an artifact due to sampling bias. For instance, an active source experiment reported the presence of a crustal magma chamber beneath the Lucky Strike segment of the MAR (Singh et

al, 2006). In addition, local Rayleigh wave imaging found slow velocities in the upper 20 km depth beneath the ridge segment studied here (Figure 1), slower in comparison to for example the segment just to the south of Chain Fracture Zone, and hypothesized the existence of upwelling and/or increased melt fraction (Saikia et al., 2021). Therefore, there is ongoing evidence that such magmatic formations are plausible even in slow-spreading ridges and thus mechanisms proposed for fast-spreading ridges may, at least partially, apply in slow-spreading ridges as well.

One additional plausible mechanism for lowering material strength to promote failure, particularly at steeply dipping faults, may be fatigue. Fatigue is a phenomenon well-known to engineers, where the strength of a material systematically decreases when repeated periodical stresses are applied. This phenomenon is typically observed in metals, but rocks can also experience fatigue (e.g. Schütz, 1996; Cerfontaine and Collin, 2017). Frohlich and Nakamura (2009) proposed fatigue as a potential mechanism for the generation of deep moonquakes, due to the tidal effects of the earth and sun in the moon's interior. Given that our study area experiences ~700 loading cycles every year, over 10^9 cycles have been completed in the last 1.5Myr, constantly subjecting the oceanic lithosphere to stress rates which are 2 orders of magnitude greater than the tectonic ones. This can potentially decrease the rock strength over time and may also explain the lack of strong events (M>6.0) in most of MAR segments. The combination of low strength, low friction and tidal loading leads to failure before sufficient stress is accumulated.

Our observations of lower b-values at high extensional stresses agrees with previous results from Axial Seamount (Tan et al., 2019), although we also found lower b-values for high extensional stress rates. Tan et al. (2019) analysed the magnitude frequency distribution of >20,000 microearthquakes within a 25 km^3 block of crust at Axial Seamount, which is subjected to tidal loading of ±20 kPa. They showed that b-values are inversely correlated with Coulomb stress, varying by ~0.09 per kPa. We could not establish a similarly robust relation in our dataset, which has over 10 times less data (1781 events above M_C). Nevertheless, we detect anomalous deviations from GR law during high tides ($|\phi|>90^o$), with the b-value varies in a way that cannot be attributed to random fluctuations and insufficient sample. Moreover, during high tides, for a 0.2 magnitude unit range the AD test even rejects the exponentiality hypothesis at 0.05 significance. We perform the Schuster test to seek for detection bias during the hours of the day. There is no significant preference at particular hours (p_s=0.20), something that is rather expected at an oceanic environment in the absence of anthropogenic noise, predominantly present during daytime in continental areas. Thus, excluding the irrational explanation that the detection level of the network decreases at high tides, our results indicate that either a periodical, tidal-induced deviation from GR law occurs at high tides, or that the selected dataset is, to some large degree, inhomogeneous. Further analysis favoured the second scenario, since proper events selection (e.g. Group 1 and Group 2, Figure 5) leads to datasets, clearly following exponential distribution, but also demonstrating significantly different b-values. Our analysis suggests that higher seismicity rates and lower b-values occur at high extensional stresses (in agreement with Tan et al., 2019) but also at high extensional stress rates.

Some very interesting conclusions also come out as we quantify the tidal effect in terms of seismic potential, incorporating the influence of both seismicity rates and magnitude distribution. In such way we find that the occurrence of large magnitude events (e.g. M≥5.0 or M≥6.0) is more likely to occur during, or towards low tides rather than during or towards high tides. Ide et al. (2016), proposed that small tidal stresses can accelerate slow deformation in various scales, and the resultant stress redistribution may increase the cascading probability of

nearly critical dynamic rupture, i.e. the probability of an event's transition from small to large scales. Such potential is clearly evident in our study, as verified by the EAR cluster analysis. The 14 EAR clusters identified have a total duration of ~1 day however, they accommodate 38.5% of the M≥2.0 events (including the 2 strongest earthquakes), or equivalently, 83% of the total seismic moment release. Figure 3b shows that EAR clusters are much more likely to initiate during or close to maximum extensional stress rate, suggesting a significant role of stress rate in initiating cascades of events, which continue as far as favourable conditions (extensional stresses) apply. This is also evident in the entire dataset, where the highest seismic activity rate is found not only during high extensional stresses ($-30^o<\phi<30^o$, Figure 3a), but also during high extensional stress rates ($-120^o<\phi<-60^o$, Figure3a). This supports fatigue as a plausible triggering mechanism, since the material strength seems to be reduced at a level that even tiny stress changes (a few kPa) are capable to induce observable variations in seismic activity. Other plausible mechanisms include the decrease in confining pressure at low tides which in turn leads to a decrease in normal stress, causing slip in mature faults (e.g. Tolstoy et al., 2002) and the tidal perturbation of fluid pressure within the cracks, caused by the overburden water load fluctuation (Stroup et al., 2009; Tolstoy et al., 2002).

5 Conclusions

We investigated the possibility of tidal triggering of microseismicity in a small volume of oceanic lithosphere at an equatorial MAR segment from ~1-year of data. Our results exhbit high statistical significance and can be summarized as follows:

1) Two groups of events can be distinguished: Group 1 comprises events that occurred during either high extensional stress or high extensional stress rates (i.e. during and towards low tides). Group 2 comprises events occurred during either high compressional stress or high compressional stress rates (i.e. during and towards high tides). Group 1 is characterized by higher activity rates and smaller b-values in comparison to Group 2.
2) 12 out of the 14 EAR clusters (seismicity bursts at remarkably high rates), belong to Group 1. All EAR clusters initiated at extensional stress rates and half of them occur very close to the maximum extensional stress rate.
3) Exceedance probabilities of strong events (M>5.0) are considerably higher in Group 1 (EP=0.28, r=8.3 events/day, b=0.80), than in Group 2 (EP=0.08, r=5.4 events/day, b=0.88).
4) Coulomb stress modelling is consistent with tidal triggering on low-angle normal faulting in a serpentinized, low-friction oceanic lithosphere.
5) Coulomb stress modelling in combination with the apparent fault plane from morphology and earthquake locations, the assumption of serpentinization at shallowest depths and also strike-slip focal mechanisms suggest additional factors such as fatigue and/or the influence of an underlying magma chamber may be required to explain the tidal triggering on high angle faults, at low tides.

Acknowledgments, Samples, and Data

C.A.R., N.H. and K.L. acknowledge funding from the Natural Environment Research Council (NE/M003507/1) and the European Research Council (GA 638665). J.-M.K. was funded by the Natural Environment Research Council (NE/M004643/1). D.S. was supported by the Portuguese Science and Technology Foundation (FCT/Fundação para a Ciência e Tecnologia), under project

PTDC/CTA-GEF/30264/2017 and UIDB/50019/2020 – IDL. We thank the captain and crew of the R/V *Marcus G. Langseth* and the RRS *Discovery*, and also the scientific technicians. The seismic data are archived at the IRIS DMC, as 2016-2017 network XS https://doi.org/10.7914/SN/XS_2016 (Rychert et al., 2016). The global seismicity data come from www.isc.ac.uk/, last accessed March 2021. Some of the moment tensors come from www.globalcmt.org/, last accessed March 2021. Figure 1 was generated using Generic Mapping Tools v.6.1.1 (www.soest.hawaii.edu/gmt, last accessed March 2021).

References

Aki, K. (1965), Maximum likelihood estimate of b in the formula logN = a − bM and its confidence limits. *Bulletin of Earthquake Research Institute of the University of Tokyo*, 43, 237–239

Agius, M. R., Harmon, N., Rychert, C. A., Tharimena, S., & Kendall, J. M. M. (2018), Sediment characterization at the equatorial Mid-Atlantic Ridge from P-to-S teleseismic phase conversions recorded on the PI-LAB experiment. *Geophysycal Research Letters*, 45, 12,244–12,252, doi: 10.1029/2018GL080565

Agius, M. R., Rychert, C. A., Harmon, N., Tharimena, S., & Kendall, J. M. (2021), A thin matnle transition zone beneath the equatorial Mid-Atlantic Ridge. *Nature*, 589, 562–566, doi: 10.1038/s41586-020-03139-x

Agnew, D. C. (1997), NLOADF: a program for computing ocean-tide loading. *Journal of Geophysical Research*, 102, 5109–5110

Barreyre, T., Escartín, J., Sohn, R. A., Cannat, M., Ballu, V., & Crawford, W. C. (2014), Temporal variability and tidal modulation of hydrothermal exit-fluid temperatures at the Lucky Strike deepsea vent field, Mid-Atlantic Ridge. *Journal of Geophysical Research: Solid Earth*, 119, 2543–2566, doi:10.1002/2013JB010478

Behn, M. D., Boettcher, M. S., & Hirth, G. (2007), Thermal structure of oceanic transform faults. *Geology*, 35, 4, 307-310, doi: 10.1130/G23112A.1

Bhatnagar, T., Tolstoy, M., & Waldhauser, F. (2015), Influence of fortnightly tides on earthquake triggering at the East Pacific Rise at 9°50′N. *Journal of Geophysical Research: Solid Earth*, 121, 1262–1279, doi:10.1002/2015JB012388

Bogiatzis, P., Karamitrou, A., Ward Neale J., Harmon, N., Rychert, C. A., & Srokosz, M. (2020), Source regions of infragravity waves recorded at the bottom of the equatorial Atlantic Ocean, using OBS of the PI−LAB experiment. *Journal of Geophysical Research: Oceans*, 125, e2019JC015430

Cann, J. R., Blackman, D. K., Smith, D. K., McAllister, E., Janssen, B., Mello, S., Avgerinos, E., Pascoe A. R. & Escartın, J. (1997), Corrugated slip surfaces formed at North Atlantic ridge-transform intersections. *Nature*, 385, 329–332

Cerfontaine, B., & Collin, F. (2017), Cyclic and fatigue behaviour of rock materials: Review, interpretation and research perspectives. *Rock Mechics and Rock Engineering*, DOI 10.1007/s00603-017-1337-5

Chamberlain, C. J., Hopp, C. J., Boese, C. M., Warren-Smith, E., Chambers, D., Chu, S. X., Michailos, K., & Townend, J. (2018), EQcorrscan: Repeating and near-repeating earthquake detection and analysis in Python. *Seismological Research Letters*, 89, 173–181

Chatelain, J. O., Roecker, S. W., Hatzfeld, D., & Molnar, P. (1980), Microearthquake seismicity and fault plane solutions in the Hindu Kush region and their tectonic implications. *Journal of Geophysical Research*, 85, 1365-1387

Cochran, E. S., Vidale J. E., & Tanaka S. (2004), Earth tides can trigger shallow thrust fault earthquakes. *Science*, 306, 1164–1166

Crawford, W. C., Rai, A., Singh, S. C., Cannat, M., Escartin, J., Wang, H., Daniel R. & Combier V. (2013), Hydrothermal seismicity beneath the summit of Lucky Strike volcano, Mid-Atlantic Ridge. *Earth and Planetary Science Letters*, 373, 118-128

Davy, R. G., Collier, J. S., Henstock, T. J., & The VoiLA Consortium (2020), Wide-Angle Seismic Imaging of Two Modes of Crustal Accretion in Mature Atlantic Ocean Crust. *Journal of Geophysical Research: Solid Earth*, 125, doi:10.1029/2019jb019100

Egbert, G. D. & Erofeeva, S. Y. (2002), Efficient inverse modeling of barotropic ocean tides. *Journal of Atmospheric and Oceanic Technology*, 19, 183-204

Engeln, J. F., Weins, D. A., & Stein, S. (1986), Mechanisms and depths of Atlantic transform earthquakes. *Journal of Geophysical Research*, 91, 548–577

Escartin, J., Hirth, G., & Evans, B. (1997), Nondilatant brittle deformation of serpentinites: Implications for Mohr-Coulomb theory and the strength of faults. *Journal of Geophysical Research*, 102, 2897–2913

Escartin, J., Hirth, G., and Evans, B. (2001), Strength of slightly serpentinized peridotites: Implications for the tectonics of oceanic lithosphere. *Geology*, 29, 1023-1026

Frohlich, C. & Nakamura, Y. (2009), The physical mechanisms of deep moonquakes and intermediate depth earthquakes: How similar and how different?. *Physics of the Earth and Planetary Interiors*, 173, 365-374, doi:10.1016/j.pepi.2009.02.004

Gibbons, S. J. & Ringdal, F. (2006), The detection of low magnitude seismic events using array-based waveform correlation, *Geophysical Journal International*, 165, 149-166, doi: 10.1111/j.1365-246X.2006.02865.x

Gravemayer, I., Reston, T. J., & Moeller, S. (2013), Microseismicity of the Mid-Atlantic Ridge at 7°S-8°15'S and at the Logatchev Massif oceanic core complex at 14°40'N-14°50'N. *Geochemistry Geophysics Geosystems*, 14, 3532-3554, doi: 10.1002/ggge.20197.

Harris, R. A. (1998), Introduction to special section: Stress triggers, stress shadows and implications for seismic hazard. *Journal of Geophysical Research*, 103, 24,347-24,358

Harmon, N., Rychert, C., Agius, M., Tharimena, S., Le Bas, T., Kendall, J. M. & Constable, S. (2018), Marine geophysical investigation of the Chain Fracture Zone in the equatorial Atlantic from the PI-LAB experiment. *Journal of Geophysical Research: Solid Earth*, 123, 11,016–11,030, doi:10.1029/2018JB015982

Harmon, N., Rychert, C. A., Kendall, J. M., Agius, M., Bogiatzis, P., & Tharimena, S. (2020), Evolution of the oceanic lithosphere in the equatorial Atlantic from Rayleigh wave tomography, evidence for small−scale convection from the PI−LAB experiment. *Geochemistry Geophysics Geosystems*, 21, e2020GC009174

Heaton, T. H. (1975), Tidal triggering of earthquakes. *Geophysical Journal International*, 43, 307-326

Heimann, S., Kriegerowski, M., Isken, M., Cesca, S., Daout, S., Grigoli, F., Juretze, C., Megies, T., Nooshiri, N., Steinberg, A., Sudhaus, H., Vasyura-Bathke, H., Willey, T., & Dahm, T. (2017), Pyrocko -an open-source seismology toolbox and library. GFZ Data Services, Potsdam, doi: 10.5880/GFZ.2.1.2017.001

Heimann, S., Isken, M., Kühn, D., Sudhaus, H., Steinberg, A., Vasyura-Bathke, H., Daout, S., Cesca, S., & Dahm, T. (2018). Grond - A probabilistic earthquake source inversion framework. V. 1.0. GFZ Data Services, Potsdam, doi: 10.5880/GFZ.2.1.2018.003

Hicks, S.P., Okuwaki, R., Steinberg, A., Rychert, C., Harmon, N., Abercrombie, R., Bogiatzis, P., Schlaphorst, D., Zahradnik, J., Kendall, J.M., Yagi, Y., Shimizu, K., & Sudhaus, H. (2020), Back-propagating supershear rupture in the 2016 Mw 7.1 Romanche transform fault earthquake. *Nature Geoscience*, 13, 647–653, doi: 10.1038/s41561-020-0619-9

Horning, G., Sohn, R. A., Canales, J. P., & Dunn, R. A. (2018), Local seismicity of the Rainbow massif on the Mid-Atlantic Ridge, Journal *of Geophysical Research: Solid Earth*, 123, 1615–1630, doi: 10.1002/2017JB015288

Hofmann, A. W. (1997), Mantle geochemistry: the message from oceanic volcanism. *Nature*, 385, 219–229.

Hough, S. E., & Kanamori, H. (2002), Source properties of earthquakes near the Salton Sea triggered by the 16 October 1999 M 7.1 Hector Mine, California, Earthquake. *Bulletin of the Seismological Society of America*, 92(4), 1281–1289, doi: 10.1785/0120000910

Hrubcová P., Doubravová, J. & Vavryčuk, V. (2021), Non-double-couple earthquakes in 2017 swarm in Reykjanes Peninsula, SW Iceland: Sensitive indicator of volcano-tectonic movements at slow-spreading rift. *Earth and Planetary Science Letters*, 563, 116875, doi: 10.1016/j.epsl.2021.116875

Ide, S., Yabe, S., & Tanaka, Y. (2016), Earthquake potential revealed by tidal influence on earthquake size–frequency statistics. *Nature*, 9, 834-838, DOI: 10.1038/NGEO2796

Laske, G., Masters, G., Ma, Z., & Pasyanos, M. (2013), Update on CRUST1.0—a 1-degree global model of Earth's crust. *Geophysical Research Abstracts*, 15, 2658

Leptokaropoulos, K. (2020), Magnitude distribution complexity and variation at The Geysers geothermal field. *Geophysical Journal International*, 222, 893-906, doi: 10.1093/gji/ggaa208

Leptokaropoulos, K. & Lasocki, S. (2020), SHAPE: A Matlab software package for time-dependent seismic hazard analysis. *Seismological Research Letters*, 91, 1867-1877, doi: 10.1785/0220190319

Linker, J., & Dieterich, J. (1992), Effects of variable normal stress on rock friction: observations and constitutive equations. *Journal of Geophysical Research*, 97, 4923–4940, doi:10.1029/92JB00017

Lomax, A., Virieux, J., Volant, P., & Berge-Thierry, C. (2000), Probabilistic earthquake location in 3D and layered models. *Advances in Seismic Event Location*, 18, 101–134

Macdonald, K. C. (2001), Mid-ocean ridge tectonics, volcanism and geomorphology. *In: Encyclopedia of Ocean Sciences, Steele, J., Thorpe, S. and Turekian, K., eds., Academic Press*, 1798-1813

Marsaglia, G. & Marsaglia, J. (2004), Evaluating the Anderson-Darling distribution. *Journal of Statistical Software*, 9, 1-5

Martínez-Garzón, P., Kwiatek, G., Bohnhoff, M., & Dresen, G. (2017), Volumetric components in the earthquake source related to fluid injection and stress state. *Geophysical Research Letters*, 44, 800–809, doi:10.1002/2016GL071963

Mercier, H., & Morin, P. (1997), Hydrography of the Romanche and Chain Fracture Zones, *Journal of Geophysical Research*, 102(C5), 10, 373–10,389, doi: 10.1029/97JC00229

Mercier, H., & Speer, K. G. (1998), Transport of bottom water in the Romanche Fracture Zone and the Chain Fracture Zone. *Journal of Physical Oceanography*, 28(5), 779–790, doi: 10.1175/1520-0485(1998)028<0779:Tobwit>2.0.Co;2

Miller, A.D., Foulger, G. R., & Julian, B. R. (1998), Non-double couple earthquakes 2. Observations. *Reviews of Geophysics*, 36, 4, 551-568

Minson, S. E., Dreger, D. S., Bürgmann, R., Kanamori, H. & Larson, K. M. (2007), Seismically and geodetically determined nondouble-couple source mechanisms from the 2000 Miyakejima volcanic earthquake swarm. *Journal of Geophysical Research*, 112, B10308, doi:10.1029/2006JB004847

Parnell-Turner, R., Sohn, R.A., Peirce, C., Reston, T. J., Macleod, C. J., Searle, R. C., & Simão, N. M. (2017), Oceanic detachment faults generate compression in extension. *Geology*, v. 45, p. 923–926, doi: 0.1130/G39232.1

Parnell-Turner, R., Sohn, R.A., Peirce, C., Reston, T. J., Macleod, C. J., Searle, R. C., & Simão, N. M. (2020), Seismicity trends and detachment fault structure at 13°N, Mid-Atlantic Ridge. *Geology*, v. 49, doi: 10.1130/G48420.1

Rice, J. R., & Cleary, M. P. (1976), Some basic stress diffusion solutions for fluid-saturated elastic porous media with compressible constituents. *Reviews of Geophysics*, 14, 227-24

Rychert, C., Kendall, J. M., & Harmon, N. (2016), Passive Imaging of the Lithosphere-Asthenosphere Boundary [Data set]. *International Federation of Digital Seismograph Networks*, https://doi.org/10.7914/SN/XS_2016

Rychert, C. A., Harmon, N., Constable, S., & Wang, S. (2020), The nature of the lithosphere−asthenosphere boundary. *Journal of Geophysical Research: Solid Earth*, 125, e2018JB016463, doi: 10.1029/2018JB016463

Saikia, U., Rychert, C., Harmon, N., & Kendall, J. M. (2020), Sediment structure at the equatorial mid-atlantic ridge constrained by seafloor admittance using data from the PI-LAB experiment. *Marine Geophysical Research*, 41, 3, doi: 10.1007/s11001-020-09402-0

Saikia, U., Rychert, C., Harmon, N., & Kendall, J. M. (2021), Upper mantle anisotropic shear velocity structure at the equatorial Mid-Atlantic ridge constrained by Rayleigh wave group velocity analysis from the PI-LAB experiment. *Geochemistry Geophysics Geosystems*, 22, e2020GC009495, doi: 10.1029/2020GC009495

Scholz, C. H., Tan, Y. J., & Albino, F. (2019), The mechanism of tidal triggering of earthquakes at mid-ocean ridges. *Nature*, 10:2526, doi: 10.1038/s41467-019-10605-2

Schuster, A. (1897), On lunar and solar periodicities of earthquakes. *Proceedings of the Royal Society of London*, 61, 455–465

Schütz, W. (1996), A history of fatigue. *Engineering Fracture Mechanics,* 54, 263–300

Simpson, R. W., & Reasenberg, P. A. (1994), *Earthquake-induced static stress changes on central California faults. In: The Loma Prieta, California Earthquake of October 17, 1989-Tectonic processes and models*, edited by R. W. Simpson U.S. Geol. Surv. Prof. Pap., 1550-F, F55-F89

Skempton, A. W. (1954), The pore-pressure coefficients A and B. Géotechnique, 4, 143-147.

Stroup, D. F., Bohnenstiehl, D. R., Tolstoy, M., Waldhauser, F., & Weekly, R. T. (2007), Pulse of the seafloor: Tidal triggering of microearthquakes at 9 degrees 50'N East Pacific Rise. *Geophyical Research Letters*, 34, L15301, doi: 10.1029/2007gl030088

Sykes, L. R. (1970) Earthquake swarms and sea-floor spreading, *Journal of Geophysical Research*, 75, 6598-6611

Tan, Y. J., Waldhauser, F., Tolstoy, M., & Wilcock, W. S. D. (2019), Axial Seamount: Periodic tidal loading reveals stress dependence of the earthquake size distribution (bvalue). *Earth and Planetary Science Letters*, 512, 39-45, doi: 10.1016/j.epsl.2019.01.047

Tanaka, S., Ohtake, M., & Sato, H. (2002), Evidence for tidal triggering of earthquakes as revealed from statistical analysis of global data. *Journal of Geophysical Research*, 107(B10), 2211, doi:10.1029/2001JB001577

Tesei, T., Harbord, C. W. A., De Paola, N., Collettini, C., & Viti, C. (2018), Friction of mineralogically controlled serpentinites and implications for fault weakness. *Journal of Geophysical Research: Solid Earth*, 123, 6976–6991, doi: 10.1029/2018JB016058.

Tolstoy, M., Vernon, F. L., Orcutt, J. A., & Wyatt, F. K. (2002), Breathing of the seafloor: Tidal correlations of seismicity at Axial volcano. *Geology*, 30 (6), 503-506

Tsuruoka, H., Ohtake, M., & Sato, H. (1995), Statistical test of the tidal triggering of earthquakes: Contribution of the ocean tide loading effect. *Geophysical Journal International*, 122(1), 183–194

Utsu, T. (1999), Representation and analysis of the earthquake size distribution: a historical review and some new approaches. *Pure and Applied Geophysics*, 155, 509-535

Vuan, A., Sugan, M., Amati, G. & Kato, A. (2018), Improving the Detection of Low−Magnitude Seismicity Preceding the Mw 6.3 L'Aquila Earthquake: Development of a Scalable Code Based on the Cross Correlation of Template Earthquakes. *Bulletin of the Seismological Society of America*, 108, 471-480, doi: 10.1785/0120170106

Waldhauser, F., & Ellsworth, W. L. (2000), A double-difference earthquake location algorithm; method and application to the northern Hayward Fault, California. *Bulletin of the Seismological Society of America*, 90, 1353–1368, doi:10.1785/0120000006

Wang, S., Constable, S., Rychert, C. A., & N., Harmon (2020), A Lithosphere−Asthenosphere Boundary and Partial Melt Estimated Using Marine Magnet-otelluric Data at the Central Middle

Atlantic Ridge. *Geochemistry Geophysics Geosystems*, 21, e2020GC009177, doi: 10.1029/2020GC009177

Wilcock, W. S. D. (2001), Tidal triggering of micro earthquakes on the Juan de Fuca Ridge. *Geophysical Research Letters*, 28, 3999–4002

Wilcock, W. S. D. (2009), Tidal triggering of earthquakes in the Northeast Pacific Ocean, *Geophysical Journal International*, 179, 1055-1070, doi: 10.1111/j.1365-246X.2009.04319.x

Wilcock, W. S. D., Tolstoy, M., Waldhauser, F., Garcia, C., Tan, Y. J., Bohnenstiehl, D. R., Caplan-Auerbach, J., Dziak, R. P., Arnulf, A. F., & Mann, M. E. (2016), Seismic constraints on caldera dynamics from the 2015 Axial Seamount eruption. *Science*, 354, 1395–1399